

Sequential phase transformations in $Ta_{0.4}Ti_2Zr$ alloy via tensile molecular dynamics simulations with deep potential

Hongyang Liu(刘洪洋), Rong Chen(陈荣), Bo Chen(陈博), Jingzhi He(贺靖之), Dongdong Kang(康冬冬), and Jiayu Dai(戴佳钰)

Citation: Chin. Phys. B, 2026, 35 (**1**): 017102. DOI: 10.1088/1674-1056/ae1e68
http://cpb.iphy.ac.cn; http://iopscience.iop.org/cpb

What follows is a list of articles you may be interested in

Anisotropic displacement threshold energy and defect distribution in diamond: PKA energy and temperature effect

Ke Wu(吴可), Zeyi Du(杜泽依), Hongyang Liu(刘洪洋), Nanyun Bao(包南云), Chengke Xu(许成科), Hongrui Wang(王泓睿), Qunchao Tong(童群超), Bo Chen(陈博), Dongdong Kang(康冬冬), Guang Wang(王广), and Jiayu Dai(戴佳钰)
Chin. Phys. B, 2025, 34 (**8**): 087104. DOI: 10.1088/1674-1056/add4f8

Unveiling the thermal transport mechanisms in novel carbon-based graphene-like materials using machine-learning potential

Yao-Yuan Zhang(章耀元), Meng-Qiu Long(龙孟秋), Sai-Jie Cheng(程赛杰), and Wu-Xing Zhou(周五星)
Chin. Phys. B, 2025, 34 (**6**): 067101. DOI: 10.1088/1674-1056/adca18

Research of caged dynamics of clusters center atoms in $Pd_{82}Si_{18}$ amorphous alloy

Yong-He Deng(邓永和), Bei Chen(陈贝), Qing-Hua Qi(祁清华), Bing-Bing Li(李兵兵), Ming Gao(高明), Da-Dong Wen(文大东), Xiao-Yun Wang(王小云), and Ping Peng(彭平)
Chin. Phys. B, 2024, 33 (**4**): 047102. DOI: 10.1088/1674-1056/ad1d4e

Atomistic simulations of graphene origami: Dynamics and kinetics

Panpan Zhang(张盼盼), Haihong Jia(贾海洪), Yan-Fang Zhang(张艳芳), and Shixuan Du(杜世萱)
Chin. Phys. B, 2023, 32 (**8**): 087107. DOI: 10.1088/1674-1056/acd527

Formation of quaternary all-d-metal Heusler alloy by Co doping fcc type Ni_2MnV and mechanical grinding induced B2-fcc transformation

Lu Peng(彭璐), Qiangqiang Zhang(张强强), Na Wang(王娜), Zhonghao Xia(夏中昊), Yajiu Zhang(张亚九),Zhigang Wu(吴志刚), Enke Liu(刘恩克), and Zhuhong Liu(柳祝红)
Chin. Phys. B, 2023, 32 (**1**): 017102. DOI: 10.1088/1674-1056/ac5e94

SPECIAL TOPIC — AI + Physical Science

Sequential phase transformations in $Ta_{0.4}Ti_2Zr$ alloy via tensile molecular dynamics simulations with deep potential

Hongyang Liu(刘洪洋)[1,2,3], Rong Chen(陈荣)[1], Bo Chen(陈博)[1,2,3,†], Jingzhi He(贺靖之)[4], Dongdong Kang(康冬冬)[1,2,3], and Jiayu Dai(戴佳钰)[1,2,3,‡]

[1] *College of Science, National University of Defense Technology, Changsha* 410073, *China*
[2] *Hunan Key Laboratory of Extreme Matter and Applications, National University of Defense Technology, Changsha*, 410073, *China*
[3] *Hunan Research Center of the Basic Discipline for Physical States, National University of Defense Technology, Changsha* 410073, *China*
[4] *College of Aerospace Science and Engineering, National University of Defense Technology, Changsha* 410073, *China*

(Received 11 October 2025; revised manuscript received 8 November 2025; accepted manuscript online 12 November 2025)

Understanding the complex deformation mechanisms of non-equimolar multi-principal element alloys (MPEAs) requires high-fidelity atomic-scale simulations. This study develops a deep potential (DP) model to enable molecular dynamics simulations of the $Ta_{0.4}Ti_2Zr$ ($Ta_{0.4}$) alloy. Monte Carlo simulations using this potential reveal Ta atom precipitation in the $Ta_{0.4}$ alloy. Under uniaxial tensile loading along the [100] direction in the NPT ensemble, the alloy undergoes a remarkable sequence of phase transformations: an initial body-centered cubic (BCC_1) to face-centered cubic (FCC) transformation, followed by a reverse transformation from FCC to a distinct BCC phase (BCC_2), and finally a BCC_2 to hexagonal close-packed (HCP) transformation. Critically, the reverse FCC to BCC_2 transformation induces significant volume contraction. We demonstrate that the inversely transformed BCC_2 phase primarily accommodates compressive stress. Concurrently, the reorientation of BCC_2 crystals contributes substantially to the observed high strain hardening. These simulations provide atomic-scale insights into the dynamic structural evolution, sequential phase transformations, and stress partitioning during deformation of the $Ta_{0.4}$ alloy. The developed DP model and the revealed mechanisms offer fundamental theoretical guidance for accelerating the design of high-performance MPEAs.

Keywords: multi-principal element alloys, machine-learning potential, phase transformation, stress partitioning

PACS: 71.15.Pd, 61.66.Dk, 02.70.Ns, 64.75.Nx

DOI: 10.1088/1674-1056/ae1e68 **CSTR:** 32038.14.CPB.ae1e68

1. Introduction

Multi-principal element alloys (MPEAs) are a new class of materials that have developed rapidly in recent years and hold broad application prospects as high-temperature structural materials in the aerospace field.[1–7] However, achieving an optimal balance between strength and ductility, coupled with a deep understanding of their complex deformation mechanisms, remains a core challenge.

To overcome the inherent ductility limitations of conventional MPEAs, researchers are actively exploring non-equimolar compositional designs to tailor microstructure and deformation behavior. For instance, Huang *et al.*[8] reduced the Ta content in the TiZrHfNb system to destabilize its phase stability, triggering a stress-induced body-centered cubic (BCC) to hexagonal close-packed (HCP) phase transformation. This phase transition generates significant work hardening via dynamic stress–strain competition between the BCC and HCP phases, promoting intragranular plastic deformation and suppressing crack initiation, thereby enhancing both strength and ductility. Similarly, Sun *et al.*[9] adjusted the Nb content in TiZrHfNb alloys to activate deformation twinning, substantially enhancing strain hardening capacity and ductility. Tong *et al.*[10] demonstrated that the addition of Zr to NbMoTaW alloys forms Zr–Zr atomic bonds, which improve both strength and plasticity. These studies collectively highlight the effectiveness of compositional adjustments — particularly atomic ratio optimization — in tailoring microstructural evolution and mechanical performance of MPEAs.

The TaTiZr system is intriguing due to its contrasting elemental phase behaviors. Titanium and zirconium exist in the HCP structure at room temperature and transform to the BCC structure at high temperature, respectively, while Ta maintains a BCC structure across a wide temperature range. This disparity in phase behavior creates opportunities to manipulate phase stability through compositional adjustments. Previous studies by Senkov *et al.*[11] revealed that slowly cooled Ta–Ti–Zr alloys develop Zr-rich (predominantly HCP) and Ta-rich (BCC) phase segregation, but increasing Ta content promotes a homogeneous BCC structure.[12] Therefore, we have chosen the

†Corresponding author. E-mail: chenbochain@nudt.edu.cn
‡Corresponding author. E-mail: jydai@nudt.edu.cn

© 2026 Chinese Physical Society and IOP Publishing Ltd. All rights, including for text and data mining, AI training, and similar technologies, are reserved.

TaTiZr system as the subject of our study, with the expectation of inducing phase transformations during deformation to enhance the mechanical properties of the alloy.

The atomic-scale origins of heterogeneous stress–strain evolution and their links to macroscopic mechanical properties in deformed non-equimolar alloys remain elusive. A deep exploration of these atomic-scale mechanisms relies heavily on high-precision computational simulations. However, existing methods exhibit significant limitations. Density functional theory (DFT), while providing quantum mechanical accuracy, suffers from prohibitive computational costs that restrict simulations to systems containing only hundreds of atoms.[13,14] Although molecular dynamics (MD) simulations are extensively utilized to investigate defect-mediated properties in multi-element alloys — including stacking faults,[15] dislocations,[16–19] twinning,[20] and phase transformations[21] — with system sizes reaching millions of atoms, their reliability critically depends on the quality of interatomic potentials. Traditional empirical potentials, despite their computational efficiency, often demonstrate insufficient accuracy due to oversimplified physical assumptions and, in particular, lack appropriate parameterizations for complex MPEA systems.[22,23]

The development of machine learning interatomic potentials (MLIPs) has emerged as a promising solution to this critical challenge. By constructing potential energy surfaces through machine learning of local atomic environments, MLIPs achieve near-DFT accuracy while maintaining computational efficiency comparable to that of classical potentials.[24–27] The importance of such high-fidelity simulations has been demonstrated in other alloy systems; for instance, Du *et al.* utilized a reactive force field to unravel the atomistic mechanism behind the rhenium strengthening effect in Ni-based superalloys.[28] This dual advantage has enabled successful applications in studying various material properties, including mechanical behavior[29] and thermodynamic characteristics of alloy systems.[30,31] Therefore, the primary task for advancing TaTiZr alloy research lies in developing specialized MLIPs that can accurately describe their complex atomic interactions and mechanical properties.

In this study, we construct a deep potential (DP) model to ensure a precise description of fundamental physical properties and interatomic interactions within the TaTiZr ternary system and its non-equimolar compositions. We employ this model to investigate tensile mechanical properties and compare the effects of random atomic distributions and Ta atom precipitation structures on the tensile response of the alloys. Our aim is to establish a clear correlation between dynamic stress partitioning phenomena and microstructural evolution, thereby revealing the underlying physical mechanisms.

2. Methods

2.1. DP model generation

Training reliable MLPs is inherently challenging due to the vast configuration space and the complexity of capturing diverse atomic interactions, particularly in MPEAs. Our approach addresses these challenges by systematically incorporating all stoichiometric ratios and employing Monte Carlo (MC)-guided sampling to explicitly explore atomic occupancy variations, thereby ensuring comprehensive coverage of local chemical environments. The DP model was developed using the deep potential generator (DP-GEN) platform,[32] which automates exploration, labeling, and training tasks (Fig. 1(a)) and has been widely applied.[33–35] The initial dataset comprised single-element, binary, and ternary equimolar alloys in BCC, face-centered cubic (FCC), and HCP phases (32 atoms per structure), with atoms randomly distributed within the alloys; ternary alloys also included amorphous structures. Meanwhile, atomic perturbations, uniaxial tension, and isotropic tension and compression deformations were applied to the structures to ensure the diversity of the initial dataset. Schematic diagrams of the deformation modes are shown in the yellow-background illustrations in Fig. 1(a).

Based on the composition ratios, the initial configurations explored by DP-GEN are classified into three categories: (i) single-element and equimolar alloys; (ii) full composition space with varying element ratios of binary alloys; and (iii) full composition space with varying element ratios of ternary alloys. The type 1, 2, and 3 configurations were converged iteratively in sequence. To avoid collecting redundant and "bad" structures, the upper limit of the force error was dynamically adjusted. During the initial iterations, the upper force error threshold was set relatively high and was gradually reduced as data accumulated. In the DP-GEN iterative process, the initial values of the upper force error threshold differed under various thermodynamic conditions. Upon final convergence, the upper force error threshold reached 0.2 eV/Å, while the lower force error threshold remained fixed at 0.1 eV/Å. Exploration of each configuration was considered converged when 95% of its dynamic trajectory configurations became accurate, with detailed iteration information provided in Table S1.

DFT calculations for labeling were performed using the Vienna *ab initio* simulation package[36,37] with an 850 eV plane-wave cutoff, 10^{-7} eV energy convergence criterion, a Monkhorst–Pack k-mesh (0.125 $Å^{-1}$ density), and the PBE-GGA functional.[38,39]

Training was performed using DeepMD-kit[40] with the se_atten[41] descriptor optimized for multielement systems (att_layer = 0). The network architecture comprised embedding layers (25, 50, 100) and fitting layers (240, 240, 240), a 6 Å cutoff radius, and learning rates ranging from 0.001 to 10^{-8}. Loss-function weights for energy, force, and

virial were set to (0.02, 1), (1000, 1), and (0.02, 1), respectively. The exploration task was performed using the Large-scale Atomic/Molecular Massively Parallel Simulator software package.[42] The final model combined the initial and iteratively generated datasets (13125 configurations) and subsequently underwent an additional 3 million training steps for further optimization.

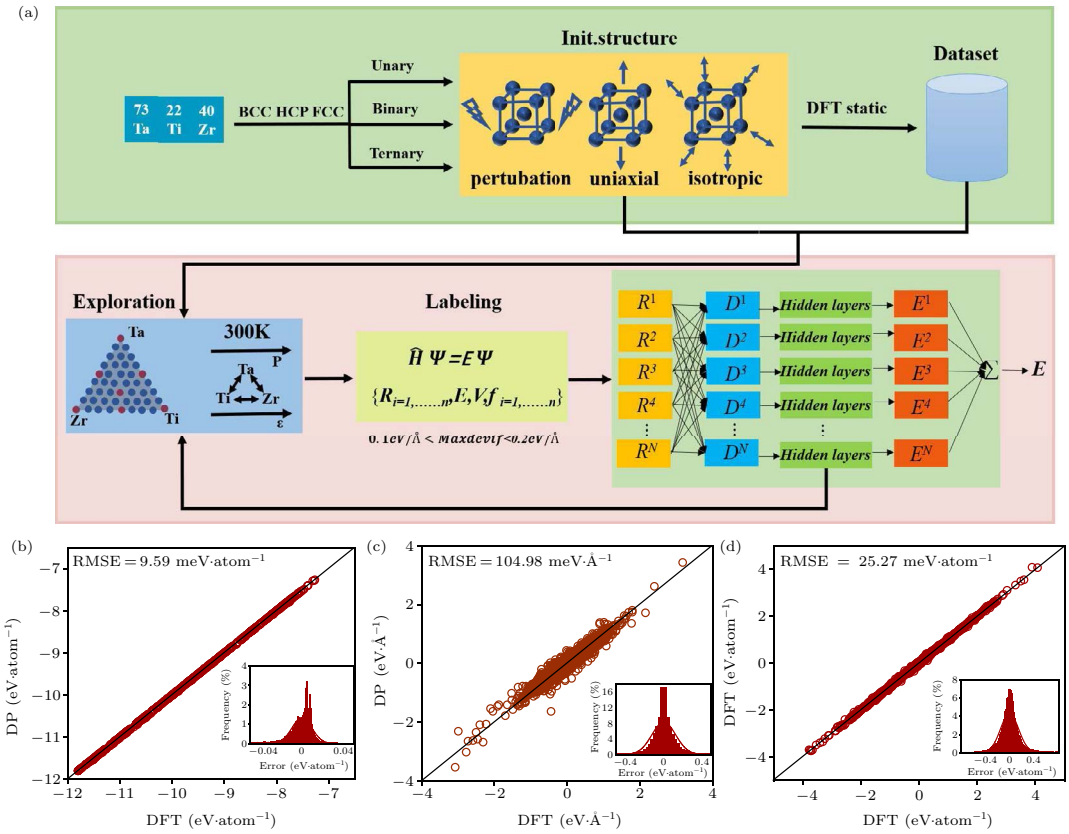


Fig. 1. Development and evaluation of the DP model. (a) Workflow for training the DP model of the ternary TaTiZr alloy. Performance of the DP model for (b) energy, (c) forces, and (d) virial stress.

2.2. MD simulations

The $Ta_{0.4}Ti_2Zr$ ($Ta_{0.4}$) alloy was investigated under the crystallographic orientations [100], [010], and [001], corresponding to the x, y, and z axes, respectively. These models were constructed by first creating a perfect BCC lattice of pure Ta, resulting in a system containing 10,976 atoms. Ti and Zr atoms were then randomly substituted for Ta atoms according to the target stoichiometry (Ta:Ti:Zr = 0.4:2:1). Prior to deformation, the supercell underwent energy minimization followed by structural relaxation in the NPT ensemble (300 K, 0 GPa, 50 ps). Uniaxial tensile deformation was applied along the z-axis ([001] direction) at a strain rate of 10^9 s^{-1} within the NPT ensemble.

Atomic ordering was quantified via the Warren–Cowley parameter (WCP)[43]

$$a_{ij} = 1 - \frac{n_{ij}}{m_j}, \tag{1}$$

where a_{ij} is the order parameter, m_j is the concentration of type j atoms, and n_{ij} is the probability of finding type j atoms in the first coordination shell of type i atoms. Structures were visualized using the Open Visualization Tool,[44] with crystal identification performed via polyhedral template matching[45] and dislocation analysis carried out using the dislocation analysis algorithm.[46]

3. Results and discussion

3.1. Deep potential model

A systematic comparison between DFT and DP predictions for energy, force, and virial stress across the training set is presented in Figs. 1(b)–1(d). The model achieved root mean squared errors (RMSEs) of 9.59 meV/atom (energy), 104.98 meV/Å (force), and 25.27 meV/atom (virial stress), with the corresponding error distributions illustrated in the inset figures, demonstrating high-precision reproduction of the DFT results.

As shown in Table 1, the DP model exhibits excellent agreement with DFT calculations for elastic constants and moduli across pure elements and alloy systems, with deviations consistently below 10%. Additional validation tests included phonon dispersion calculations for three elemental systems and equation-of-state analyses for elemental and binary alloys (see Figs. S1 and S2, respectively). The strong con-

sistency between the DP results and the DFT calculations or available literature data demonstrates the accuracy of the DP model. Notably, the binary alloy structures used for validation were obtained from the Materials Project database[47] and were not included in the training set. The successful performance of the model on these unseen configurations demonstrates its robust generalization capability beyond the training domain.

Table 1. Elastic constants (C_{ij}), bulk modulus (B), shear modulus (G) and Poisson's ratio (μ) predicted by the DP model.

		C_{11} (GPa)	C_{12} (GPa)	C_{13} (GPa)	C_{33} (GPa)	C_{44} (GPa)	B (GPa)	G (GPa)	ρ (g·cm^{-3})	μ
Ta	DFT/Exp.	272.2	176.5	176.5	272.2	77.4	208.4	65.6	16.3[48]	0.36
	DP	287.3	164.2	164.2	287.3	71.1	205.3	67.3	16.6	0.35
Ti	DFT/Exp.	170.7	87.1	78.1	181.6	42.3	111.9	44.1	4.5[48]	0.33
	DP	165.4	88.1	75.1	173.5	49.8	109.0	45.4	4.6	0.32
Zr	DFT/Exp.	140.4	66.5	64.4	155.9	28.4	92.5	35.3	6.5[48]	0.33
	DP	134.2	68.1	69.1	162.5	30.4	93.7	33.8	6.5	0.34
$Ta_{0.4}$	DFT/Exp.	137.8	98.5	102.4	131.3	39.8	113.1	28.0	6.5	0.39
	DP	127.2	96.5	101.4	115.1	39.2	107.1	30.7	6.6	0.40

3.2. The effect of the Ta atom precipitation

Atomic distribution patterns in MPEAs critically influence their mechanical performance.[16,20] To investigate this phenomenon in Ta-containing systems, we first examined emergent ordering behaviors in the $Ta_{0.4}$ alloy. Figure 2(a) shows the energy evolution and atomic distribution characteristics of the $Ta_{0.4}$ alloy. From the energy curve, it can be seen that after convergence, the single-atom energy decreases by 26.96 meV, clearly indicating a more energetically favorable and stable configuration. The left and right panels in Fig. 2(a) correspond to the random and the MC/MD-relaxed structures before and after energy convergence, respectively, highlighting the structural evolution induced by atomistic rearrangements. A clear precipitation of Ta atoms is observed in the MC/MD structure, suggesting preferential clustering of Ta within specific regions of the alloy lattice. The WCP values for each atomic pair are shown in Fig. 2(b). In the random structure, the WCP values are close to zero, indicating a random distribution of atoms in the $Ta_{0.4}$ alloy. After performing MC/MD simulations based on the random structure, the WCP value of the Ta–Ta atomic pair in Fig. 2(b) is −3.53, which quantitatively indicates the precipitation tendency of Ta–Ta atomic pairs and their strong mutual attraction. Similar Ta atom segregation has been reported in other systems, such as HfNbTa and HfNbTaTiZr alloys.[49,50] Compared with the initial random structure, the WCP values for Ta–Ti and Ta–Zr atomic pairs increase, indicating a certain repulsive interaction between Ta–Ti and Ta–Zr atomic pairs in the $Ta_{0.4}$ alloy after MC/MD simulations, which consequently results in fewer Ta atoms in the immediate vicinity of Ti and Zr atoms. Meanwhile, the WCP values for Zr–Zr, Ti–Zr, and Ti–Ti atomic pairs remain close to zero, indicating no significant attraction or repulsion among these pairs, and their distributions remain statistically disordered throughout the lattice.

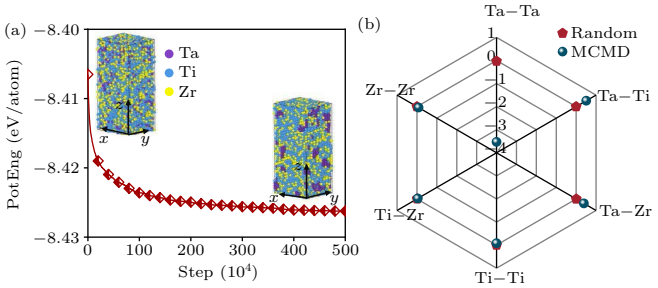


Fig. 2. Potential energy, atomic configurations, and WCP parameters of $Ta_{0.4}$ during iterative MC/MD simulations at 300 K. (a) Energy evolution of the system and atomic structures at the initial and final states of the MC/MD process. (b) WCP values of atom pairs at the initial and final states.

3.3. Stress-strain curve under NPT ensemble

Figures 3(a1) and 3(a2) show the stress–strain curves of the $Ta_{0.4}$ alloy under the NPT ensemble when subjected to 50% tensile strain along the [100] direction. By comparing the slopes of the elastic segments, it is apparent that the MC/MD structure exhibits a marginally higher elastic modulus and yield strength than the random structure. This behavior is attributed to the interfacial mismatch between Ta precipitates and Ti/Zr-rich regions, which leads to increased interfacial friction. As the strain increases, the stress initially rises linearly, reaches a maximum value, and then decreases to form a stress plateau. Following the plateau, the stress continues to decrease with increasing strain and subsequently rises again after reaching a minimum value. Notably, the stress becomes negative in the d–f region of Figs. 3(a1) and 3(a2), consistent with prior observations in other alloys.[51,52]

The evolution of the phase structure during the tensile process is depicted in Figs. 3(b1) and 3(b2). The random structure exhibits a higher fraction of the BCC phase than the MC/MD structure. Given that HCP is the stable structure for Ti and Zr at room temperature, lattice sites occupied by Ti and Zr provide more nucleation sites for the HCP phase. Consequently, the proportion of the HCP phase in the MC/MD structure is higher than that in the random structure. With increas-

ing tensile strain, these initial HCP regions gradually grow and provide early-stage plasticity. This phenomenon has also been observed in $Co_{25}Ni_{25}Fe_{25}Al_{7.5}Cu_{17.5}$.[53] Meanwhile, the extent of the BCC (BCC_1) to FCC phase transformation in the random structure is higher than that in the MC/MD structure (a–c in Figs. 3(b1) and 3(b2)). The HCP content in the MC/MD structure remains higher than that in the random structure, while the increase in HCP is mainly attributed to the growth of pre-existing HCP regions. Similar BCC–FCC phase transformations along the [100] direction have been reported in previous studies on HfNbTaTiZr,[54] Ta,[55] and Mo nanowires.[56] As the strain continues to increase, the FCC phase fraction rapidly decreases, whereas the BCC phase fraction increases significantly, accompanied by a clear reverse transformation from FCC to BCC (BCC_2). Subsequently, a BCC_2 to HCP phase transformation occurs, as indicated by the yellow line in Figs. 3(b1) and 3(b2). Experimentally, BCC–HCP phase transformations have been observed in similar systems such as $HfNbxTa_{0.2}TiZr$[57] and HfTaxTiZr.[8] Continuous phase transformations play an important role in improving the mechanical properties of alloys. Tsianikas *et al.*[58] introduced small atoms such as B, C, and O into a BCC-phase FeMnCoCr alloy, which modulated phase stability and induced a continuous transformation from BCC to HCP and then to FCC. The resulting HCP/FCC nanolayers enhanced plasticity through strain partitioning. Lu *et al.*[59] proposed a new twinning mechanism that exploits the metastable nature of the FCC phase to induce an FCC-to-HCP transformation, forming FCC twins within the HCP phase. Chen *et al.*[60] achieved a transformation from FCC to HCP in CoCrNi, followed by a reversal to FCC via twinning, which improved the ductility of the alloy.

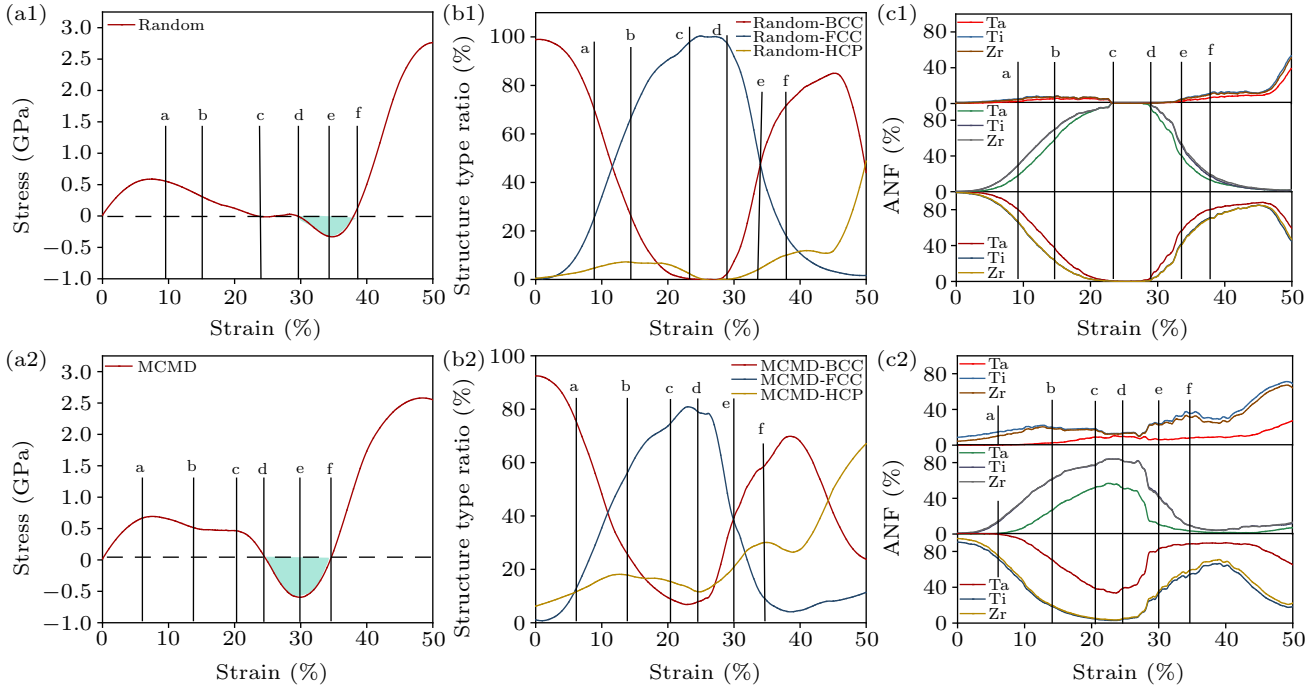


Fig. 3. Stress–strain behavior, phase-type fractions, and atomic number fractions (ANF) of Ta, Ti, and Zr for BCC, FCC, and HCP phases. (a1)–(c1) Random structure. (a2)–(c2) MC/MD structure.

The metastable nature of the FCC phase makes it difficult for conventional characterization methods to capture the continuous phase transformation process of BCC_1–FCC–BCC_2. Therefore, the results obtained in this study remain predictive and require further careful experimental validation. For this purpose, we have designed the following comprehensive experimental plan: first, high-purity $Ta_{0.4}Ti_2Zr$ alloy ingots will be prepared using a vacuum melting furnace under controlled conditions to minimize contamination; subsequently, electron backscatter diffraction (EBSD) and energy dispersive spectroscopy (EDS) techniques will be employed to identify grains with suitable orientations and target compositions, and a focused ion beam (FIB) will be used to extract usable micro- or nanoscale samples for detailed analysis. During tensile deformation, the structural evolution within individual grains will be observed in real time by transmission electron microscopy (TEM), providing direct visualization of the evolving phases, while stress partitioning mechanisms among different phases will be investigated by *in-situ* neutron diffraction experiments, following the approach demonstrated in studies such as that by Bae *et al.*,[52] and the effects of different compositions on the mechanical properties of the alloy will be systematically considered and quantified. This part of the work will be carried out in subsequent research.

From point d to e in Figs. 3(a1), 3(a2), 3(b1), and 3(b2), the FCC phase gradually decreases, while the compressive

stress correspondingly increases. At point e in Figs. 3(a1) and 3(a2), the compressive stress reaches its maximum, and at this specific strain, the BCC and FCC phase contents are equal (Figs. 3(b1) and 3(b2)). Subsequently, the compressive stress gradually decreases as the strain further increases. At point f, the stress returns to zero (Figs. 3(a1) and 3(a2)). Meanwhile, within the d–f strain range, the reverse phase transformation from FCC to BCC_2 occurs, corresponding to two opposing stress trends that indicate complex stress redistribution within the material. Statistical analysis of the elemental composition of the $Ta_{0.4}$ alloy during the tensile process is shown in Figs. 3(c1) and 3(c2). It is evident that Ta is the primary constituent of the BCC phase, while Ti and Zr atoms are the predominant components of the FCC and HCP phases, regardless of whether the structure is random or MC/MD. In the random structure, the BCC phase disappears when the strain is between 23.22% and 28.8% (indicated by c–d in Fig. 3(c1)), with the structure fully transformed into the FCC phase. In contrast, the MC/MD structure always retains a fraction of the BCC phase, which is composed exclusively of precipitated Ta atoms (Fig. 3(c2)), highlighting the stabilizing effect of Ta segregation on the BCC phase during tensile deformation.

3.4. Tensile-induced phase transformations

The phase evolution of the random and MC/MD structures under tensile deformation is analyzed in Fig. 4, with atomic configurations (a)–(f) corresponding to the strain points marked in the strain–structure type ratio curves of Fig. 3(b1) and 3(b2). In the random structure, the FCC and HCP phases are initially homogeneously distributed (Fig. 4(a1)). As the strain increases, BCC_1 rapidly transforms into FCC (Fig. 4(b1)), culminating in near-complete FCC dominance at point d (Fig. 3(b1)), illustrating the dynamic nature of phase conversion. Subsequent strain increase (Figs. 4(e1) and 4(f1)) triggers the inverse transformation from FCC to BCC_2, sharply reducing the FCC fraction and demonstrating the reversible nature of the phase transition. For the MC/MD structure, segregation of Ta from the matrix promotes localized Ti/Zr-rich regions, which serve as preferential nucleation sites for HCP phase formation, resulting in a higher initial HCP fraction (Fig. 4(a2)). Continuous straining induces substantial FCC phase growth concurrent with stacking fault formation (Figs. 4(b2) and 4(d2)), while sustained deformation ultimately drives FCC-to-BCC_2 reversion (Figs. 4(e2) and 4(f2)). Notably, Ta-rich regions (circled in Figs. 4(a2) and 4(f2)) maintain a stable BCC phase throughout the deformation process, demonstrating the critical role of Ta in localized phase stabilization and suggesting potential avenues for tailoring alloy performance through controlled Ta distribution.

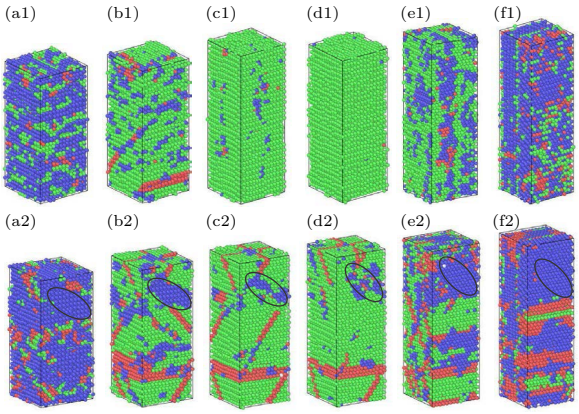


Fig. 4. Phase structure distribution of $Ta_{0.4}$ at different strains along the [100] crystallographic direction in the NPT ensemble. (a1)–(f1) Random structure. (a2)–(f2) MC/MD structure. Letters correspond to those in Fig. 3. Atoms colored in blue, green, and red represent BCC, FCC, and HCP structures, respectively.

3.5. Volume change during deformation

To investigate the anomalous negative stress regime observed during tensile deformation, the volume change of the $Ta_{0.4}$ alloy is illustrated in Fig. 5. Under tensile loading, the alloy exhibits progressive volumetric expansion (Fig. 5(a)). A detailed analysis of volume variations correlated with the light green shaded regions in Figs. 3(a1) and 3(a2) reveals a distinct trend (Fig. 5(b)): both the random and MC/MD structures exhibit an initial contraction followed by expansion with increasing strain. This volume response implies a transition in the internal stress state from tensile to compressive within the anomalous negative stress regime. A similar phenomenon was observed by Li *et al.*[51] during the tensile deformation of the CoNiFeAlCu alloy, which was attributed to a sharp drop in stress caused by volume expansion along the tensile direction. The minimum volume point corresponds to the state at which the contents of the BCC and FCC phases are equal. Thereafter, with further increasing strain, the BCC phase content exceeds that of the FCC phase, and the volume increases again because the volume expansion induced by tensile deformation outweighs the volume contraction associated with the phase transformation.

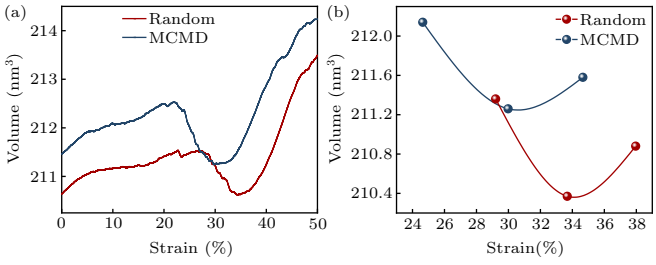


Fig. 5. (a) Volume change as a function of tensile strain. (b) Volume evolution corresponding to strain points d, e, and f in Figs. 3(a1) and 3(a2).

3.6. Stress distribution in BCC, FCC, and HCP phases

The atomic stress distribution in the BCC, FCC, and HCP phases was investigated under three strain conditions (green

regions in Figs. 3(a1) and 3(a2)). At strains corresponding to points d and f (Fig. 3), the peak atomic stresses in all phases approach zero, consistent with the zero-stress states observed in the stress–strain curves (Figs. 3(a1) and 3(a2)). Notably, the BCC phase exhibits predominantly negative atomic stresses at strain point e (Figs. 6(b1) and 6(b2)), revealing that the BCC phase primarily accommodates compressive stress during deformation. Although both the random and MC/MD structures show similar stress distribution patterns, the MC/MD structure demonstrates significantly higher compressive stress magnitudes than the random structure, reflecting its enhanced volume contraction. This contraction is further intensified by Ta atom precipitation during deformation. Figure S3 presents the stress distributions of the BCC, FCC, and HCP phases for both the random and MC/MD structures at a tensile strain of 45%. It can be observed that during the strain-hardening stage, both the BCC and HCP phases are subjected to tensile stress.

3.7. Phase transformation mechanism

To explore the phase transformation mechanism underlying the pronounced volume contraction in the BCC phase of the MC/MD structure, the evolution of crystal orientation during deformation was analyzed at three critical strains (24.64%, 29.98%, and 34.66%, corresponding to points d, e, and f in Fig. 3(a2)). Orientation mapping (Figs. 7(a1)–7(a3)) reveals a reversible transformation from BCC_1 (with [100] parallel to the tensile direction) to FCC and subsequently to BCC_2 (with $[0\bar{1}1]$ parallel to the tensile direction). The initial BCC_1 to FCC transformation follows the classical Bain path[61] along the [001] direction (Figs. 7(b1) and 7(b2)), consistent with observations in ZrNb alloys.[62] This mechanism involves lattice expansion along the tensile axis coupled with contraction in the perpendicular directions, thereby reaching a critical axial ratio that triggers FCC phase formation. The FCC→BCC_2 transformation follows the Pitsch orientation relationship[63] (Figs. 7(c1) and 7(c2)), involving coordinated lattice rotation and tensile deformation. First, the $(110)_{FCC}$ plane rotates by 19.5° about the [001] axis, and the $[1\bar{1}0]_{FCC}$-oriented atoms are transformed into $[1\bar{1}1]_{BCC}$. Second, tensile deformation occurs along the $[001]_{FCC}$ direction.

By comparing the phase fractions of the disordered and MC/MD structures, as well as the phase constitution of precipitated Ta atoms during tensile deformation, it can be concluded that Ta plays a crucial role in stabilizing the BCC phase. In practical alloy design, phase stability can therefore be tailored by adjusting the Ta content, thereby influencing mechanical properties through phase transformation behavior. The BCC_1 to FCC transformation along the Bain path exhibits pronounced strain-softening behavior, facilitating deformation at reduced stress levels and serving as a potential mechanism for enhancing plasticity. During the reverse FCC to BCC_2 transformation, the stress–strain response evolves through a tension–compression–tension sequence, in which volumetric contraction-induced stress relaxation shifts the local stress state from tensile to compressive. This transition mechanism enables effective stress redistribution, alleviating stress concentrations and potentially improving alloy ductility.

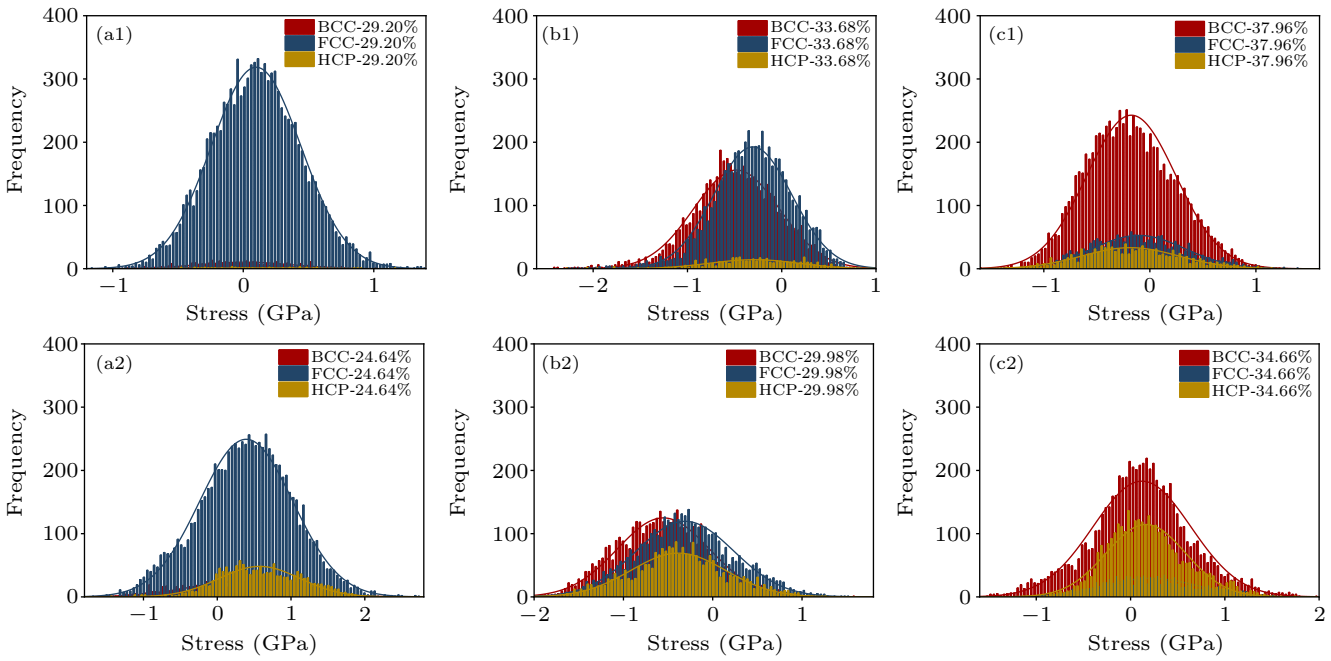


Fig. 6. Atomic stress distribution in different phases. (a1)–(c1) Random structure. (a2)–(c2) MC/MD structure. Panels (a1)–(c1) show the z-direction normal stress distribution for BCC, FCC, and HCP phases under 29.2%, 33.68%, and 37.68% strain, respectively. Panels (a2)–(c2) show the z-direction normal stress distribution for BCC, FCC, and HCP phases in the MC/MD structure under 24.64%, 29.98%, and 34.66% strain, respectively.

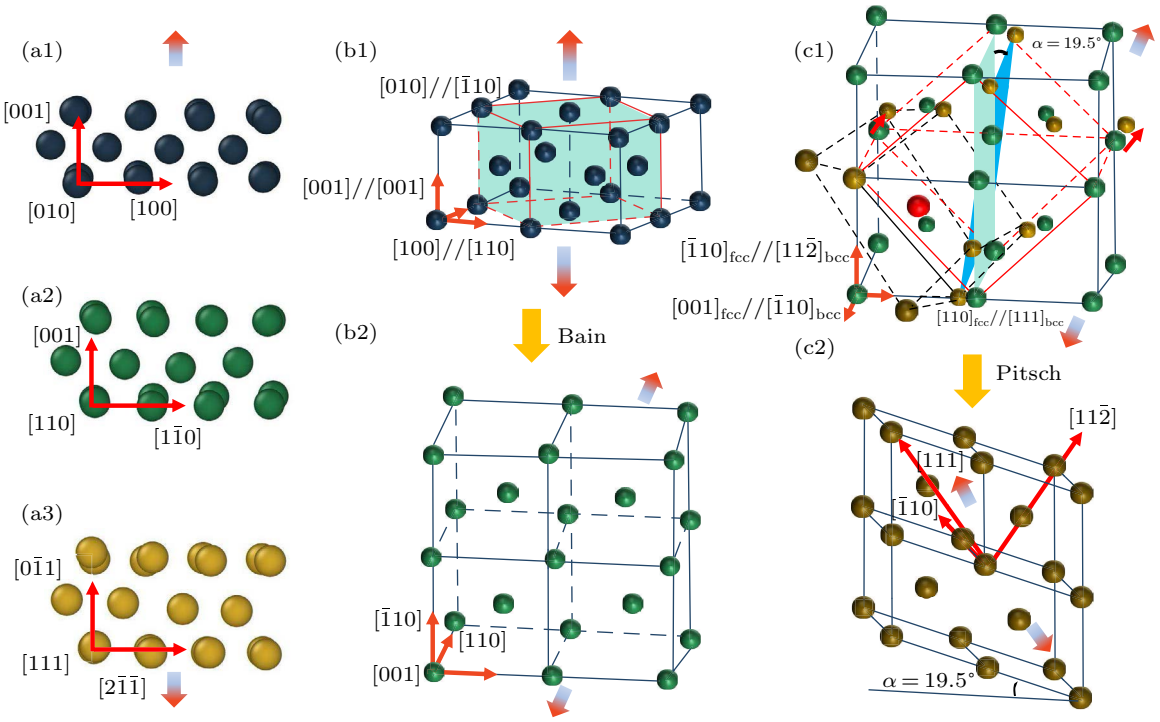


Fig. 7. Crystal orientation relationships and phase transition mechanisms. (a1)–(a3) BCC_1–FCC–BCC_2 phase transition. (b1)–(b2) Bain orientation relationship. (c1)–(c2) Pitsch orientation relationship. Dark blue atoms represent the initial BCC phase (BCC_1), green atoms represent FCC phase atoms, and orange atoms represent atoms formed by the FCC-to-BCC reverse phase transition (BCC_2).

Additionally, the newly formed BCC_2 phase preferentially aligns along the [0$\bar{1}$1] direction. The reverse phase transformation observed during deformation effectively acts as a carrier for energy relaxation. As external work is applied to the material, the internal energy of the system increases, providing the driving force for the formation of metastable structures. This unstable intermediate phase serves not only to relax excess energy but also to facilitate crystallographic reorientation and accommodate plastic deformation. The tensile stress–strain curve along the [0$\bar{1}$1] crystallographic orientation (Fig. S4) reveals a greater resistance to lattice slip compared to tensile loading along the [100] direction. Combined with the phase-resolved stress distribution at 45% strain shown in Fig. S3, these results indicate that both BCC crystal reorientation and the BCC–HCP phase transformation jointly contribute to the alloy's strain hardening behavior. These microscopic mechanisms are therefore expected to provide key guidance for the design of high-performance alloys.

3.8. Dislocation density during tensile deformation

During tensile deformation along the [100] direction, the BCC phase remains largely dislocation-free, whereas the FCC phase exhibits a high dislocation density dominated by $(1/6)\langle 112\rangle$ Shockley partials, which are frequently associated with stacking faults exhibiting HCP-like structural characteristics. In the random structure, the dislocation density initially increases and then decreases prior to point c in Fig. 8(a), confirming that the HCP phase predominantly manifests as stacking faults, consistent with the observations in Fig. 4(b1). In the c–d region (Fig. 8(a)), FCC-phase dislocations vanish concurrently with a negligible HCP fraction. Subsequently, within the d–f strain interval, the dislocation density increases

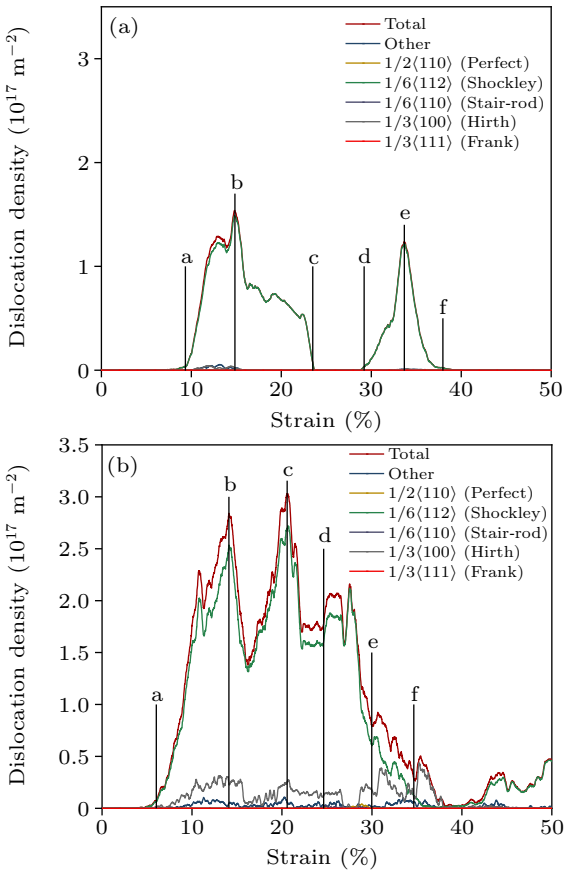


Fig. 8. Dislocation density in the FCC phase. (a) Random structure, (b) MC/MD structure. Points a–f correspond to the same strain points a–f in Fig. 3.

and then drops to zero, in contrast to the continuous growth of the HCP phase shown in Fig. 3(b1), indicating that BCC-to-HCP transformation becomes dominant at higher strain levels.

In contrast, the MC/MD structure exhibits significantly higher densities of Shockley partial dislocations than the random structure (Fig. 8(b)). Dislocations nucleate as early as point a, peak at points b and c, and reach a local minimum at approximately 16.2% strain. Between 35.76% and 50% strain, persistently low dislocation densities are accompanied by a rapid increase in the HCP phase fraction (Fig. 3(b2)), demonstrating that HCP phase formation proceeds primarily through the consumption of the BCC phase. The evolution of FCC phase dislocations at representative strain levels is further detailed in Fig. S5.

4. Summary

In summary, we have developed and validated a high-precision DP model for the TaTiZr system. After MC/MD treatment, Ta atoms precipitate within the $Ta_{0.4}$ structure. This precipitation lowers the system's energy, stabilizing the structure and slightly increasing both the elastic modulus and yield strength. Under uniaxial tension along the [100] crystallographic direction, the FCC phase, acting as an intermediate phase, facilitates the reorientation of the BCC phase from [001] BCC_1 to $[0\bar{1}1]$ BCC_2 along the loading direction. The reoriented BCC_2 phase induces significant volume contraction. Notably, as strain progresses, the lattice exhibits increased resistance to deformation along the $\langle 110 \rangle$ direction relative to $\langle 100 \rangle$. This directional anisotropy drives a fundamental transition in the local stress state from compressive to tensile dominance, ultimately contributing to the observed strain-hardening behavior.

Acknowledgments

This work was supported by the National University of Defense Technology Research Fund Project, the National Natural Science Foundation of China (Grant No. 12534013), and the Science and Technology Innovation Program of Hunan Province (Grant Nos. 2025ZYJ001 and 2021RC4026).

References

[1] Zhang Z, Zhang H, Tang Y, Zhu L, Ye Y, Li S and Bai S 2017 *Mater. Des.* **133** 435
[2] Senkov O N, Senkova S V, Woodward C and Miracle D B 2013 *Acta Mater.* **61** 1545
[3] Senkov O N, Wilks G B, Scott J M and Miracle D B 2011 *Intermetallics* **19** 698
[4] Senkov O N, Scott J M, Senkova S V, Meisenkothen F, Miracle D B and Woodward C F 2012 *J. Mater. Sci.* **47** 4062
[5] Zherebtsov S, Yurchenko N, Shaysultanov D, Tikhonovsky M and Stepanov N 2020 *Adv. Eng. Mater.* **22** 2000105
[6] Eleti R R, Stepanov N and Zherebtsov S 2020 *Scr. Mater.* **188** 118
[7] Mills L H, Emigh M G, Frey C H, Philips N R, Murray S P, Shin J, Gianola D S and Pollock T M 2023 *Acta Mater.* **245** 118618
[8] Huang H, Wu Y, He J, Wang H, Liu X, An K, Wu W and Lu Z 2017 *Adv. Mater.* **29** 1701678
[9] Wang S, Shu D, Shi P, Zhang X, Mao B, Wang D, Liaw P K and Sun B 2024 *J. Mater. Sci. Technol.* **187** 72
[10] Tong Y, Bai L, Liang X, Chen Y, Zhang Z, Liu J, Li Y and Hu Y 2020 *Intermetallics* **126** 106928
[11] Senkov O N, Kuhr S J, Shank J M, Payton E J and Woodward C 2021 *Mater. Sci. Eng. A* **814** 141168
[12] He J, Tang Y, Zhang Z, Li S, Ye Y, Luo H and Bai S 2022 *Corros. Sci.* **209** 110778
[13] Zhang C, Xie S, Li X, Sun R, Liu B, Liu W, Yu Q, Xiong H, Zhang R and Yin H 2024 *J. Alloys Compd.* **992** 174578
[14] Wu Y, Zhang Y, Li Z, Liu Z, Zhao E and Liu J 2024 *J. Mater. Res. Technol.* **30** 8854
[15] Lu J, Wang J, Wan K, Chen Y, Wang H and Shi X 2023 *J. Chem. Phys.* **158** 204702
[16] Wang T, Li J, Wang M, Li C, Su Y, Xu S and Li X G 2024 *npj Comput. Mater.* **10** 143
[17] Yin S, Zuo Y, Anas A O, Hui Z, Li X, Ding J, Ong S P, Asta M and Ritchie R O 2021 *Nat. Commun.* **12** 4873
[18] Zhao L, Zong H, Ding X and Lookman T 2021 *Acta Mater.* **209** 116801
[19] Zhou X, Wu H, Wu Y, Liu X, Peng X, Hou S and Lu Z 2024 *Acta Mater.* **281** 120364
[20] Santos-Florez P A, Dai S, Yao Y, Yanxon H, Li L, Wang Y, Zhu Q and Yu X 2023 *Acta Mater.* **255** 119041
[21] Kostiuchenko T, Körmann F, Neugebauer J and Shapeev A 2019 *npj Comput. Mater.* **5** 55
[22] Ferrari A, Körmann F, Asta M and Neugebauer J 2023 *Nat. Comput. Sci.* **3** 221
[23] Wen T, Zhang L, Wang H, Weinan E and Srolovitz D J 2022 *Mater. Futures* **1** 022601
[24] Chang X, Chen B, Zeng Q, Wang H, Chen K, Tong Q, Yu X, Kang D, Zhang S and Guo F 2024 *Nat. Commun.* **15** 8543
[25] Zeng Q, Chen B, Zhang S, Kang D, Wang H, Yu X and Dai J 2023 *npj Comput. Mater.* **9** 213
[26] Chang X, Kang D, Chen B and Dai J 2025 *Chin. Phys. Lett.* **42** 053704
[27] Qiu R, Zeng Q, Han J, Chen K, Kang D, Yu X and Dai J 2025 *Phys. Rev. B* **111** 064103
[28] Du W, Fan X, Xiao B, Sun J, Wang Q, Tang Y, Zhang L, Goddard W A and Liu Y 2025 *Acta Mater.* **285** 120712
[29] Li X, Chen C, Zheng H, Zuo Y and Ong S P 2020 *npj Comput. Mater.* **6** 10
[30] Xiao R, Wang Q, Qin J, Zhao J, Ruan Y, Wang H, Li H and Wei B 2023 *J. Appl. Phys.* **133** 085102
[31] Zhou Y, Srinivasan P, Körmann F, Grabowski B, Smith R, Goddard P and Duff I A 2022 *Phys. Rev. B* **105** 214302
[32] Zhang Y, Wang H, Chen W, Zeng J, Zhang L, Wang H and Weinan E 2019 *Comput. Phys. Commun.* **253** 107206
[33] Yang F, Zeng Q, Chen B, Kang D, Zhang S, Wu J, Yu X and Dai J 2022 *Chin. Phys. Lett.* **39** 116301
[34] Han J, Zeng Q, Chen K, Yu X and Dai J 2023 *Nanomaterials* **13** 1576
[35] Guo F, Chen B, Zeng Q, Yu X, Chen K, Kang D, Du Y, Wu J and Dai J 2023 *J. Chem. Phys.* **159** 204702
[36] Kresse G and Furthmüller J 1996 *Comput. Mater. Sci* **6** 15
[37] Kresse G and Furthmüller J 1996 *Phys. Rev. B* **54** 11169
[38] Perdew J P, Burke K and Ernzerhof M 1996 *Phys. Rev. Lett.* **77** 3865
[39] Kresse G and Joubert D 1999 *Phys. Rev. B* **59** 1758
[40] Zeng J, Zhang D, Lu D, Mo P, Li Z, Chen Y, Rynik M, Huang L A, Li Z and Shi S 2023 *J. Chem. Phys.* **159** 054801
[41] Zhang D, Bi H, Dai F, Jiang W, Liu X, Zhang L and Wang H 2024 *npj Comput. Mater.* **10** 94
[42] Plimpton S 1995 *J. Comput. Phys.* **117** 1
[43] Cowley J M 1950 *Phys. Rev.* **77** 669
[44] Stukowski A 2009 *Modell. Simul. Mater. Sci. Eng.* **18** 015012
[45] Larsen P M, Schmidt S and Schiøtz J 2016 *Modell. Simul. Mater. Sci. Eng.* **24** 055007
[46] Stukowski A 2012 *Modell. Simul. Mater. Sci. Eng.* **20** 045021
[47] Jain A, Ong S P, Hautier G, Chen W, Richards W D, Dacek S, Cholia S, Gunter D, Skinner D and Ceder G 2013 *APL Mater.* **1** 011002
[48] Kittel C and McEuen P 2018 *Introduction to Solid State Physics*, 8th edn. (Beijing: Chemical Industry Press) pp. 16 (in Chinese)
[49] Chen Y, Feng H, Li J, Liu B, Jiang C, Liu Y, Fang Q and Liaw P K 2024 *Proc. Natl. Acad. Sci. USA* **121** 1

[50] Xun K, Zhang B, Wang Q, Zhang Z, Ding J and Ma E 2023 *J. Mater. Sci. Technol.* **135** 221
[51] Li J, Fang Q, Liu B and Liu Y 2018 *Acta Mater.* **147** 35
[52] Bae J W, Jung J, Kim J G, Park J M, Harjo S, Kawasaki T, Woo W and Kim H S 2020 *Materialia* **9** 100619
[53] Wu Y and Shao J 2023 *Int. J. Plast.* **169** 103730
[54] Wei J and Lu R 2023 *Int. J. Plast.* **173** 103867
[55] Pan Z, Li Y and Wei Q 2008 *Acta Mater.* **56** 3470
[56] Mostafa A, Vu L, Guo Z, Shargh A K, Dey A, Askari H and Abdolrahim N 2024 *Comput. Mater. Sci* **244** 113273
[57] Wen X, Wu Y, Huang H, Jiang S, Wang H, Liu X, Zhang Y, Wang X and Lu Z 2021 *Mater. Sci. Eng. A* **805** 140798
[58] Tsianikas S, Chen Y, Jeong J, Zhang S and Xie Z 2021 *Nanoscale* **13** 3602
[59] Lu S, Sun X, Tian Y, An X, Li W, Chen Y, Zhang H and Vitos L 2023 *PNAS Nexus* **2** pgac282
[60] Chen Y, Chen D, An X, Zhang Y, Zhou Z, Lu S, Munroe P, Zhang S, Liao X and Zhu T 2021 *Acta Mater.* **215** 117112
[61] Sandoval L, Urbassek H M and Entel P 2009 *New J. Phys.* **11** 103027
[62] An K, Ou X and Song M 2022 *J. Nonferrous Met.* **32** 2989
[63] Cayron C 2013 *Acta Crystallogr. A* **69** 498